

1     **Variability of visual field maps in human early extrastriate cortex challenges**  
2             **the canonical model of organization of V2 and V3**

3             Fernanda L. Ribeiro<sup>a,b\*</sup>, Ashley York<sup>a,b</sup>, Elizabeth Zavitz<sup>c,d</sup>, Steffen Bollmann<sup>e</sup>,  
4                     Marcello G. P. Rosa<sup>c,d¶</sup>, Alexander M. Puckett<sup>a,b¶</sup>

5  
6     ***Affiliations:***

7     <sup>a</sup> School of Psychology, The University of Queensland; Brisbane QLD 4072; Australia

8     <sup>b</sup> Queensland Brain Institute, The University of Queensland; Brisbane QLD 4072;  
9     Australia

10    <sup>c</sup> Department of Physiology, Monash University; Clayton VIC 3800; Australia

11    <sup>d</sup> Neuroscience Program, Biomedicine Discovery Institute; Monash University; Clayton  
12    VIC 3800; Australia

13    <sup>e</sup> School of Information Technology and Electrical Engineering, The University of  
14    Queensland; Brisbane QLD 4072; Australia

15    <sup>¶</sup> Joint senior authors

16    \* Corresponding author: [fernanda.ribeiro@uq.edu.au](mailto:fernanda.ribeiro@uq.edu.au)

17 **Abstract**

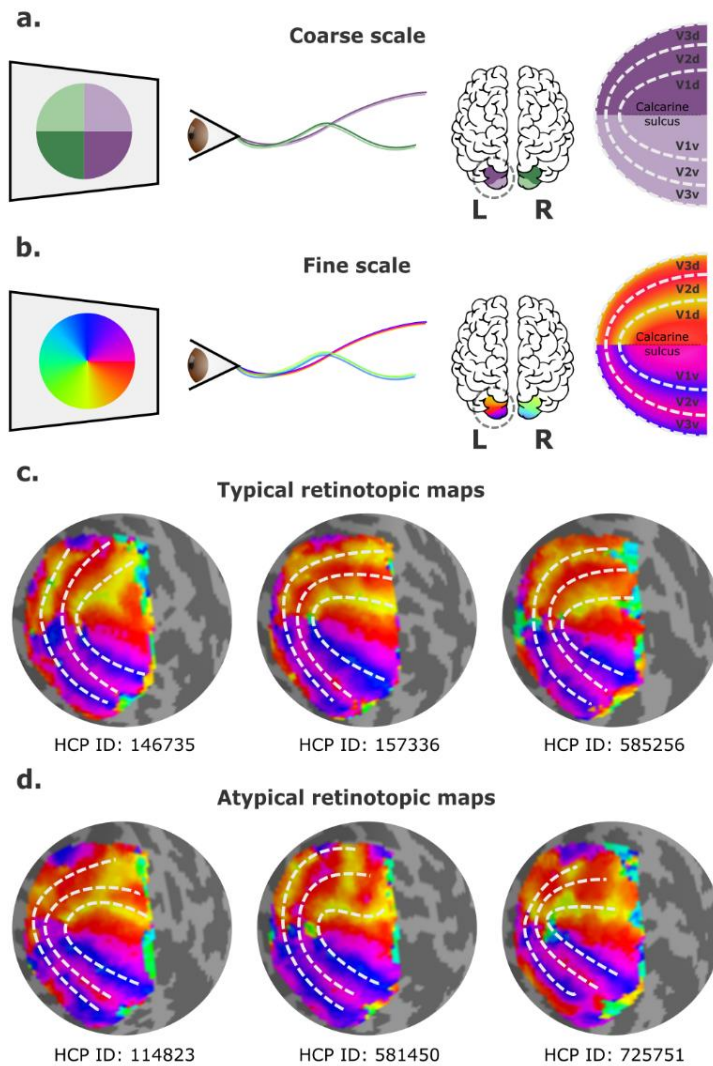
18 Visual field maps in human early extrastriate areas (V2 and V3) are traditionally  
19 thought to form mirror-image representations which surround the primary visual cortex  
20 (V1). According to this scheme, V2 and V3 form nearly symmetrical halves with  
21 respect to the calcarine sulcus, with the dorsal halves representing the lower  
22 contralateral quadrants, and the ventral halves representing the upper contralateral  
23 quadrants. This arrangement is considered to be consistent across individuals, and  
24 thus predictable with reasonable accuracy using templates. However, data that  
25 deviate from this expected pattern have been observed, but mainly treated as  
26 artifactual. Here we systematically investigate individual variability in the visual field  
27 maps of human early visual cortex using the large-scale 7T Human Connectome  
28 Project (HCP) retinotopy dataset. Our results demonstrate substantial and principled  
29 inter-individual variability in early visual retinotopy. Visual field representation in the  
30 dorsal portions of V2 and V3 were more variable than their ventral counterparts,  
31 including substantial departures from the expected mirror-symmetrical patterns.  
32 Surprisingly, only one-third of individuals had maps that conformed to the expected  
33 pattern. In addition, retinotopic maps in the left hemisphere were more variable than  
34 those in the right hemisphere. Our findings challenge the current view that inter-  
35 individual variability in early extrastriate cortex is negligible, and that the dorsal  
36 portions of V2 and V3 are roughly mirror images of their ventral counterparts.

37 **Keywords**

38 human connectome project, retinotopy, high-resolution fMRI, 7T, vision, hemispheric  
39 differences, V3

## 40 **Introduction**

41 Non-invasive imaging has been instrumental in mapping the topographic organization  
42 of human visual cortex (Wandell and Winawer, 2010). The visual field maps in early  
43 visual areas (V1, V2, and V3) have been reported to be remarkably consistent across  
44 people, and predictable with reasonable accuracy using a template (Benson et al.,  
45 2014, 2012; Schira et al., 2010). While V1 contains a complete, first-order (continuous)  
46 representation of the contralateral visual hemifield, areas V2 and V3 form second-  
47 order (discontinuous) representations (Rosa, 2002). In these areas, a field  
48 discontinuity near the horizontal meridian splits the maps into upper and lower field  
49 representations that are only connected at the foveal confluence (Figure 1a,b).  
50 Accordingly, in parcellation schemes (Glasser et al., 2016; Wang et al., 2015), early  
51 visual areas form concentric bands, arranged in nearly symmetrical halves with  
52 respect to the calcarine sulcus. These bands, each containing the representation of a  
53 contralateral visual field quadrant, are referred to as the dorsal and ventral portions of  
54 V2 and V3 (Figure 1a). However, observations originating in several laboratories has  
55 indicated departures from this pattern, particularly in the dorsal region (Allen et al.,  
56 2021; Arcaro and Kastner, 2015; Benson and Winawer, 2018; Van Essen and Glasser,  
57 2018). Even so, small-sized datasets, variability in acquisition sites and protocols, and  
58 methodological constraints have limited the investigation of this variability. As a result,  
59 no consensus exists about deviations from the canonical mirror-symmetrical  
60 organization of V2 and V3.



61

62 **Figure 1 – Visual field mapping in the human early visual cortex.** **a**, Coarse scale  
63 visual field mapping in the early visual cortex. The left (L) hemisphere maps the right  
64 visual field, and the right (R) hemisphere maps the left visual field. The dorsal portion  
65 of early visual areas maps the lower hemifield, and the ventral portion the upper field.  
66 **b**, Fine scale visual field mapping with visual field maps represented in polar angles  
67 (0-360°). The vertical (90° or 270°) and horizontal meridians (0° for the left and 180°  
68 for the right hemispheres) delineate boundaries between visual areas. **c**, Three  
69 “typical” polar angle maps, obtained from the left hemispheres of three individuals in  
70 the HCP retinotopy dataset, which conform to the traditional model. **d**, Three polar  
71 angle maps that deviate from this pattern, obtained from left hemispheres of three  
72 other individuals in the HCP retinotopy dataset. In the latter, the isopolar bands  
73 representing the anterior borders of dorsal V3 (V3d) and dorsal V2 (V2d) do not follow  
74 the proposed borders of V2 and V3 (dashed lines).

75 In humans, empirical visual field mapping using functional MRI (fMRI) is the primary  
76 means of delineating precise visual area boundaries in individuals. Visual field maps  
77 are typically defined in polar coordinates, resulting in two maps: one representing polar  
78 angle (or clock position) and the other eccentricity (or distance away from the fixation  
79 point) (Wandell and Winawer, 2010). In primates, isoangle bands representing the  
80 vertical and the horizontal meridians are thought to delineate boundaries between V1  
81 and V2, V2 and V3, and V3 and higher-order visual areas (Figure 1b). Particularly, in  
82 human probabilistic maps, boundaries between the dorsal portions of early visual  
83 areas are roughly mirror images of their ventral counterparts (Figure 1c).  
84 Nevertheless, boundaries that deviate from the expected ones exist, but these have  
85 been mainly treated as artifactual, with researchers often overlooking the irregularities  
86 by simply drawing the boundaries to resemble that of a typical map as best as possible  
87 (Figure 1d). Here, it may be important to remark that the border between the dorsal  
88 parts of V2 and V3 is well known to be variable in other mammals, and that it typically  
89 does not coincide with the representation of the horizontal meridian (see Rosa and  
90 Manger, 2005 for review).

91 Although previous reports of individual variability in the dorsal portion of human early  
92 visual cortex were primarily anecdotal (Allen et al., 2021; Arcaro and Kastner, 2015;  
93 Benson and Winawer, 2018; Van Essen and Glasser, 2018), a recently developed  
94 deep learning model predicts that individual variability in retinotopy exists, and that this  
95 is correlated with variations in gross anatomy (e.g., the pattern of sulci and gyri)  
96 (Ribeiro et al., 2021). Moreover, studies modelling the formation of retinotopic maps  
97 in non-human primates also indicate that different variants could develop based on  
98 application of similar rules (Yu et al., 2020).

99 Motivated by these findings, here we systematically investigate individual variability in  
100 visual field maps of human early visual cortex using a recently released, large-scale  
101 dataset: the 181 participants, 7T Human Connectome Project (HCP) retinotopy  
102 dataset (Benson et al., 2018). Our aims were to quantify the level of individual  
103 variability throughout early visual cortex (V1-V3) and to determine whether there are  
104 common modes of retinotopic organization that differ from the established view (i.e.,  
105 whether individual retinotopic maps differ from a template in similar ways). Our results  
106 challenge the current view that individual differences in retinotopic organization reflect  
107 experimental artifacts that may be dismissed for practical purposes. In particular, they  
108 demonstrate that the dorsal portions of human early visual areas are more  
109 heterogeneous than previously acknowledged.

## 110 **Materials and Methods**

### 111 ***Dataset***

112 We used the Human Connectome Project (HCP) 7T Retinotopy dataset (Benson et  
113 al., 2018) to investigate individual variability in retinotopic maps of human early visual  
114 cortex. This dataset consists of high-resolution functional retinotopic mapping and  
115 structural data from 181 participants (109 females, age 22-35) with normal or  
116 corrected-to-normal visual acuity. Participant recruitment and data collection were led  
117 by Washington University and the University of Minnesota. The Institutional Review  
118 Board (IRB) at Washington University approved all experimental procedures (IRB  
119 number 201204036; “Mapping the Human Connectome: Structure, Function, and  
120 Heritability”), and all participants provided written informed consent before data

121 collection (Van Essen et al., 2013). Additionally, the acquisition protocol has been  
122 described in previous work (Benson et al., 2018; Van Essen et al., 2013).

123 Structural data were acquired at 0.7 mm isotropic resolution in a customized Siemens  
124 3T Connectome scanner (Van Essen et al., 2013). Briefly, cortical surfaces were  
125 reconstructed from T1w structural images using FreeSurfer and aligned to the 32k  
126 fs\_LR standard surface space. This standard 32k fs\_LR cortical surface consists of  
127 32,492 vertices sparsely connected, forming triangular faces. Functional data were  
128 later aligned with this standard surface space.

129 Functional retinotopic mapping data were acquired using a Siemens 7T Magnetom  
130 scanner at 1.6 mm isotropic resolution and 1 s TR. Data were preprocessed following  
131 the HCP pipeline (Glasser et al., 2013), which included correction for head motion and  
132 EPI spatial distortion, alignment of the fMRI data with the HCP standard surface space,  
133 and denoising for spatially specific structured noise. Retinotopic mapping stimuli  
134 comprised rotating wedges, expanding and contracting rings, and bars of different  
135 orientations moving across different directions in the visual field. A population  
136 receptive field (pRF) modeling procedure was then used to reconstruct visual field  
137 maps (Benson et al., 2018; Dumoulin and Wandell, 2008; Kay et al., 2013), which  
138 encompasses estimating the spatial preference of cortical surface vertices to different  
139 locations of the visual field (i.e., its receptive field) defined in polar coordinates – for  
140 more, see Benson et al, (2018). Hence, polar angle maps are retinotopic maps  
141 reflecting the polar angle (angle relative to the horizontal vertical meridian) in the visual  
142 field to which a vertex is most responsive, while eccentricity maps reflect the distance  
143 from the center of the visual field (i.e., the fixation point). The combination of a polar  
144 angle map and an eccentricity map completely specifies a map of the visual field.

145 ***Region of Interest***

146 Early visual areas were defined by a surface-based probabilistic atlas (Wang et al.,  
147 2015). This probabilistic atlas includes the dorsal and ventral portions of V1, V2 and  
148 V3, not including the foveal confluence. For the clustering analysis, we slightly  
149 modified the atlas by extending the dorsal border of V3 and including V1/V2/V3 foveal  
150 confluence (Schira et al., 2009), in line with our previous work (Ribeiro et al., 2021).

151 ***Individual variability***

152 We determined individual variability in visual field maps to quantify how variable these  
153 maps were across visual areas (V1, V2, and V3), portions (dorsal and ventral), and  
154 hemispheres (left and right) in human early visual cortex. First, we computed the  
155 average retinotopic maps across all 181 individuals from the HCP retinotopy dataset  
156 for both left and right hemispheres. Then, we iteratively calculated the vertex-wise  
157 difference between an individual's retinotopic map and the average map. The  
158 difference between two angles is given by:

159 
$$\text{MIN} (|\hat{\theta} - \theta|, |\hat{\theta} - \theta + 2\pi|, |\hat{\theta} - \theta - 2\pi|) \quad (1)$$

160 for  $0 < \theta < 2\pi$ .

161 Finally, vertex-wise difference scores were averaged over vertices in the range of 1-  
162 8° of eccentricity within the dorsal and ventral portions of early visual areas, resulting  
163 in one scalar value per individual per visual area, which we refer to as the individual  
164 variability. The eccentricity mask was defined using the group-average eccentricity  
165 map. This range of eccentricity values was chosen because, in the original population  
166 receptive field mapping experiment of the HCP, the visual stimulus extended to 8° of  
167 eccentricity (Benson et al., 2018). Additionally, due to the inherent difficulty in mapping



168 the foveal confluence (Schira et al., 2009), we constrained our comparison to  
169 eccentricity values above 1°. According to studies in non-human primates, this  
170 corresponds approximately to half of the expected extent of V1, V2 and V3 (Gattass  
171 et al., 1988, 1981).

## 172 ***Linear mixed-effects model***

173 We determined whether there were main effects and interactions of hemispheres (left,  
174 right), visual areas (V1, V2, V3), and portions (dorsal, ventral) on individual variability  
175 of retinotopic maps using linear mixed-effect (LME) models. Standard ANOVAs and t-  
176 tests assume statistical independence of individuals' data (Yu et al., 2022), which is  
177 often not the case. For example, the 7T HCP retinotopy dataset includes data from 50  
178 monozygotic and 34 dizygotic twins, totaling 168 individuals out of 181. Therefore, to  
179 meet the statistical independence criterion, many data points would have to be  
180 disregarded for standard statistical inference. However, LME models allow us to take  
181 full advantage of the dataset by explicitly modeling cluster-specific means (random  
182 intercepts). Indeed, individual variability from different visual areas is naturally  
183 clustered by individuals (Magezi, 2015). Therefore, using this statistical model, we can  
184 appropriately model individual-specific effects (Magezi, 2015; Yu et al., 2022).

185 In our linear mixed effect model, the dependent variable is the individual variability ( $Y$ ),  
186 which is modeled as a function of the fixed effects ( $\beta$ ) of three factors ( $x$ ) and their  
187 interactions. These three factors are: hemisphere, visual area, and portion.  
188 Additionally, we also consider the random effects ( $\gamma_i$ ) associated with the individual ( $i$   
189 = 1, ..., 181), and the random effects of each factor nested within the individual ( $\gamma_{ij}$ ,  
190 with  $j = 1, 2,$  and  $3$ ). This model is expressed as:

191 
$$Y_i = \beta_0 + \sum_{j=1}^3 \beta_j x_j + \beta_{12} x_1 x_2 + \beta_{13} x_1 x_3 + \beta_{23} x_2 x_3 + \beta_{123} x_1 x_2 x_3 + \sum_{j=1}^3 \gamma_{ij} + \gamma_i + \varepsilon_i$$

192 where  $\beta_0$  is the intercept and  $\varepsilon$  is the residual random error. We built two separate  
193 models for individual variability associated with polar angle and eccentricity maps  
194 using Jamovi (“The jamovi project (2021),” n.d.).

### 195 ***Clusters of spatial organization***

196 Lastly, we performed an exploratory clustering analysis to determine whether  
197 retinotopic maps differ from the average map in similar ways, particularly in the dorsal  
198 portion of early visual cortex. Specifically, we investigated the spatial overlap between  
199 retinotopic maps as an unambiguous indicator of the similarity between two maps.  
200 First, to obtain such a measure of the spatial overlap, the continuous polar angle maps  
201 were converted into discrete maps, such that each vertex was categorized into one  
202 out of four possible labels:

203 
$$\theta_{discrete} = \begin{cases} 0^\circ, & \text{for } 0^\circ \leq \theta_{continuous} \leq 45^\circ \\ 90^\circ, & \text{for } 45^\circ < \theta_{continuous} \leq 180^\circ \\ 270^\circ, & \text{for } 180^\circ \leq \theta_{continuous} < 315^\circ \\ 360^\circ, & \text{for } 315^\circ \leq \theta_{continuous} < 360^\circ \end{cases}$$

204 these categories were chosen because they highlight the location of visual area  
205 boundaries. Discrete eccentricity maps were determined by:

206 
$$\theta_{discrete} = \begin{cases} 0^\circ, & \text{for } 0^\circ \leq \theta_{continuous} \leq 2^\circ \\ 2^\circ, & \text{for } 2^\circ < \theta_{continuous} \leq 4^\circ \\ 4^\circ, & \text{for } 4^\circ < \theta_{continuous} \leq 6^\circ \\ 6^\circ, & \text{for } 6^\circ < \theta_{continuous} \end{cases}$$

207 Next, the spatial overlap between discrete maps from all possible pairs of individuals  
208 was estimated using the Jaccard similarity coefficient (Levandowsky and Winter, 1971;  
209 Taha and Hanbury, 2015). The Jaccard index estimates similarity between two maps

210 by taking the size of the intersection (in number of vertices) divided by the size of the  
211 union of two label sets. Hence, the Jaccard score ranges from 0 to 1; the closer to 1  
212 the score is, the more similar the two maps are. For our data and each pair of  
213 individuals, the Jaccard index is determined from the two possible individuals'  
214 combinations (i.e., individual 1 vs. individual 2 and individual 2 vs. individual 1) since  
215 the order of the maps determines which map is the reference one. For each  
216 combination, we estimated the Jaccard index for each label, and their weighted  
217 average was determined using the number of labels' instances in the reference map  
218 to account for label imbalance. Then, these two estimates were averaged, resulting in  
219 one estimate of the spatial overlap between two individuals' discrete retinotopic maps.

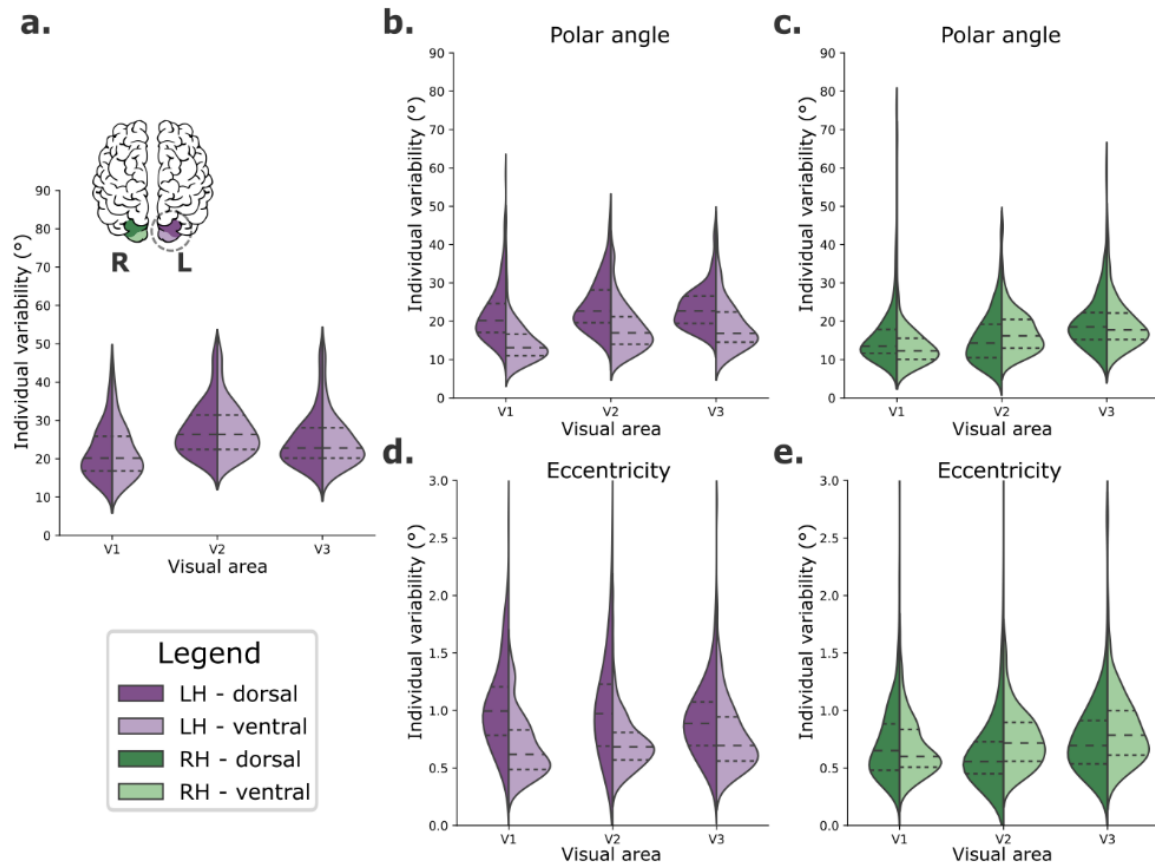
220 To assess whether inter-individual differences fell into stereotyped patterns, we  
221 applied a spectral clustering algorithm from Scikit-learn (Abraham et al., 2014;  
222 Pedregosa et al., 2011). This algorithm operates on the low-dimensional embedding  
223 of the affinity matrix (our Jaccard index-based similarity matrix), followed by K-means  
224 clustering of the components of the eigenvectors in the low-dimensional space. This  
225 low dimensional space is determined by selecting the most relevant eigenvectors of  
226 the graph Laplacian of the affinity matrix, of which corresponding eigenvalues reflect  
227 important properties of the affinity matrix that can be used to partition it (Luxburg,  
228 2007). In implementing the spectral clustering algorithm, we set the number of clusters  
229 to 6 and fixed the random state for replication purposes. We selected this number of  
230 clusters as there are at least five different models of third-tier visual cortex organization  
231 in non-human primates (Angelucci and Rosa, 2015), with a sixth cluster intended to  
232 capture noisy or unclear retinotopic organization. After clustering, we computed each  
233 cluster's mean map by averaging the continuous retinotopic maps across individuals  
234 within each cluster.

235 ***Data and code availability***

236 The data used in this study is publicly available at BALSAs  
237 (<https://balsa.wustl.edu/study/show/9Zkk>). All accompanying Python source code will  
238 be available upon publication on GitHub.

239 **Results**

240 We defined an individual variability metric to quantify how variable visual field maps  
241 are across visual areas (V1, V2, and V3), portions (dorsal and ventral), and  
242 hemispheres (left and right) in human early visual cortex. First, we computed the  
243 average visual field maps across all 181 individuals from the HCP retinotopy dataset  
244 for both left and right hemispheres. Then, we iteratively calculated the difference  
245 between an individual's visual field map and the average map. Finally, these  
246 differences were averaged over all vertices within the dorsal and ventral portions of  
247 early visual areas, resulting in one scalar value per individual per visual area, which is  
248 our individual variability metric. Figure 2 shows the distribution of individual variability  
249 scores across all participants.



250

251 **Figure 2 – Individual variability in visual field maps of early visual areas. a,**  
252 Hypothetical diagram of symmetrical distributions of individual variability across visual  
253 areas. Empirical distributions of individual variability of polar angle (b and c) and  
254 eccentricity (d and e) maps for both dorsal (dark shades) and ventral (lighter shades)  
255 portions of early visual areas in left (purple) and right (green) hemispheres.

256 We built a linear mixed effect model (Yu et al., 2022) to test the fixed effects of  
257 hemispheres, visual areas, and portions on individual variability of polar angle (Table  
258 1) and eccentricity (Table 2) maps. Table 1 shows statistically significant main effects  
259 of all factors on individual variability of polar angle maps. Specifically, polar angle  
260 maps of the left hemisphere show higher individual variability than those found in the  
261 right hemisphere (mean difference = 3.35,  $p < .001$ ). The dorsal portions of early visual  
262 areas are also more variable than the ventral portions (mean difference = 3.30,  
263  $p < .001$ ). Finally, post-hoc comparisons of visual areas indicated that V3 has higher

264 individual variability than V2 (mean difference = 1.60,  $p < .001$ ) and V1 (mean difference  
265 = 3.99,  $p < .001$ ); V2 also has higher individual variability than V1 (mean difference =  
266 2.38,  $p < .001$ ). For brevity, we only show the main effects in Table 1, although we also  
267 found statistically significant interactions. Briefly, each visual area in the left  
268 hemisphere has significantly higher individual variability than its analogous area in the  
269 right hemisphere. In addition, the dorsal portion of each visual area of the left  
270 hemisphere is significantly more variable than its dorsal analogue in the right  
271 hemisphere and the ventral analogue of both the left and right hemispheres (for more,  
272 see the Supplementary Material). These findings suggest that individual variability in  
273 polar angle representations varies across hemispheres, visual areas, and according  
274 to dorsal/ventral locations.

275 **Table 1 - Fixed effects parameter estimates for the linear mixed effect model of**  
276 **individual variability of polar angle maps.** SE – standard error; CI – confidence  
277 interval.

Polar angle								
Names	Effect	Estimate	SE	95% CI		df	t	p
				Lower	Upper			
Intercept	Intercept	18.58	0.30	17.99	19.17	180	61.86	<.001
Hemisphere	RH-LH	-3.35	0.32	-3.97	-2.72	181	-10.47	<.001
Visual area (1)	V2-V1	2.38	0.29	1.81	2.95	210	8.21	<.001
Visual area (2)	V3-V1	3.99	0.32	3.36	4.61	187	12.54	<.001
Portion	ventral - dorsal	-3.30	0.29	-3.86	-2.74	181	-11.50	<.001

278

279 Moreover, Table 2 shows statistically significant main effects of the hemisphere, visual  
280 area, and the visual area portion on individual variability of eccentricity maps. Like  
281 polar angle maps, eccentricity maps of the left hemisphere show higher individual  
282 variability than those in the right hemisphere (mean difference = 0.14,  $p < .001$ ). The  
283 dorsal portion of early visual areas is also more variable than the ventral portion (mean  
284 difference = 0.13,  $p < .001$ ). For visual areas, post-hoc comparisons indicated that the  
285 only statistically significant difference was that of V3 versus V1, with V3 having higher  
286 individual variability than V1 (mean difference = 0.05,  $p < .004$ ). In addition, statistically  
287 significant interactions were also found (Supplementary Material). Each visual area in  
288 the left hemisphere has significantly higher individual variability than analogous areas  
289 in the right hemisphere, except for V3. Eccentricity maps of each visual area's dorsal  
290 portion in the left hemisphere are significantly more variable than the dorsal

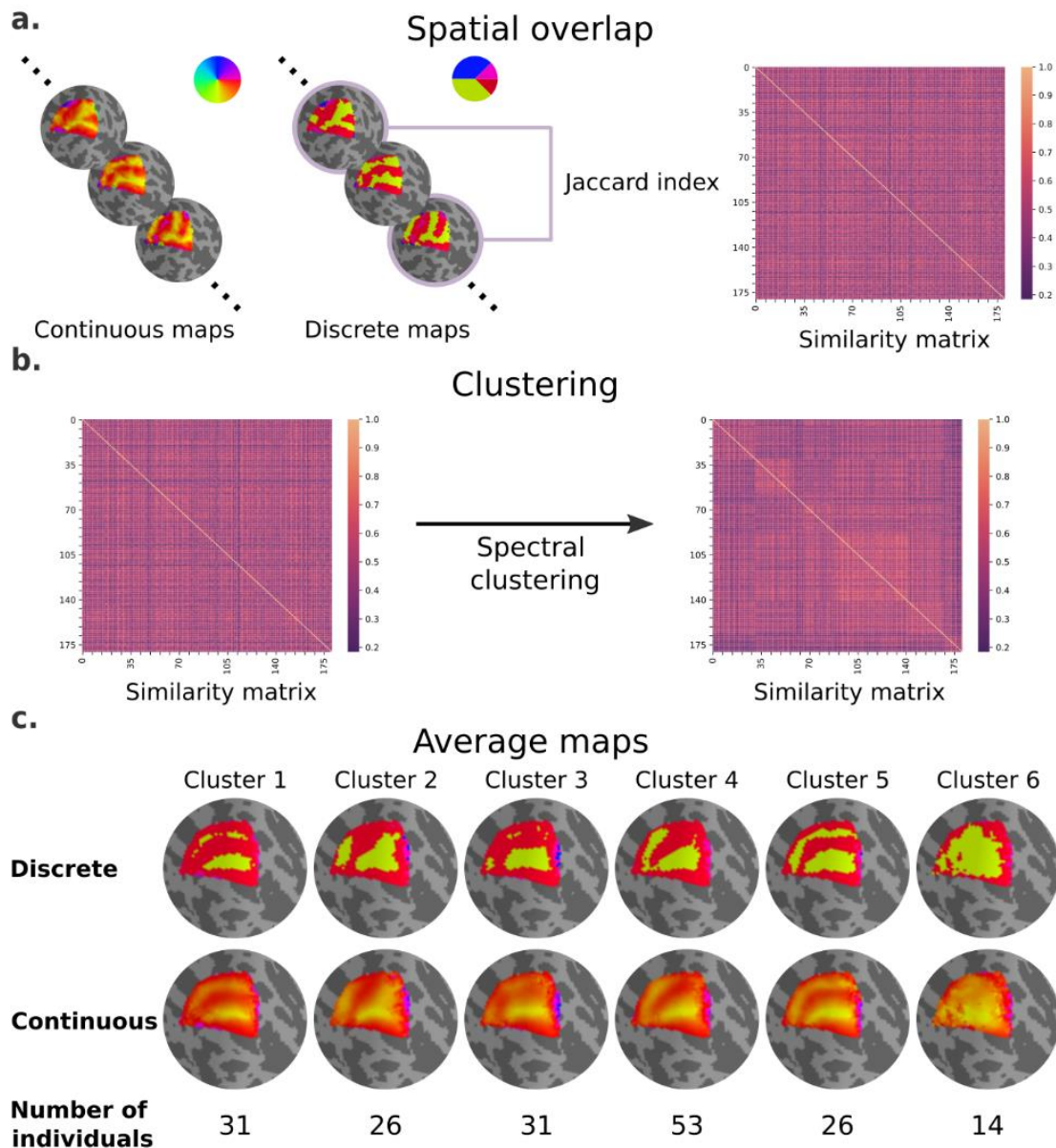
291 counterpart in the right hemisphere, and the ventral analogues in both the left and the  
292 right hemispheres.

293 **Table 2 – Fixed effects parameters estimates for the linear mixed model of**  
294 **individual variability of eccentricity maps.** SE – standard error; CI – confidence  
295 interval.

Eccentricity								
Names	Effect	Estimate	SE	95% CI		df	t	p
				Lower	Upper			
Intercept	Intercept	0.81	0.02	0.77	0.85	180	41.86	<.001
Hemisphere	RH-LH	-0.14	0.01	-0.16	-0.11	181	-10.91	<.001
Visual area (1)	V2-V1	0.01	0.01	-0.01	0.04	402	0.98	0.326
Visual area (2)	V3-V1	0.05	0.01	0.02	0.08	182	3.24	0.001
Portion	ventral - dorsal	-0.13	0.03	-0.18	-0.07	180	-4.64	<.001

296 Next, we performed an exploratory analysis to determine whether retinotopic maps  
297 differ from the average map in similar ways, particularly in the dorsal portion of early  
298 visual cortex of the left hemisphere. We focus on results for polar angle maps here as  
299 no meaningful differences were observed across eccentricity map clusters  
300 (Supplementary Figure 1). We computed the extent of overlap between discrete polar  
301 angle maps from all possible pairs of individuals using the Jaccard index, resulting in  
302 a similarity matrix (Figure 3a). Next, we applied a spectral clustering algorithm with a  
303 fixed number of clusters equal to 6 (Figure 3b). Finally, we averaged the continuous  
304 polar angle maps across individuals within each cluster to visualize common patterns  
305 of retinotopic organization in the dorsal portion of early visual cortex (Figure 3c).





306

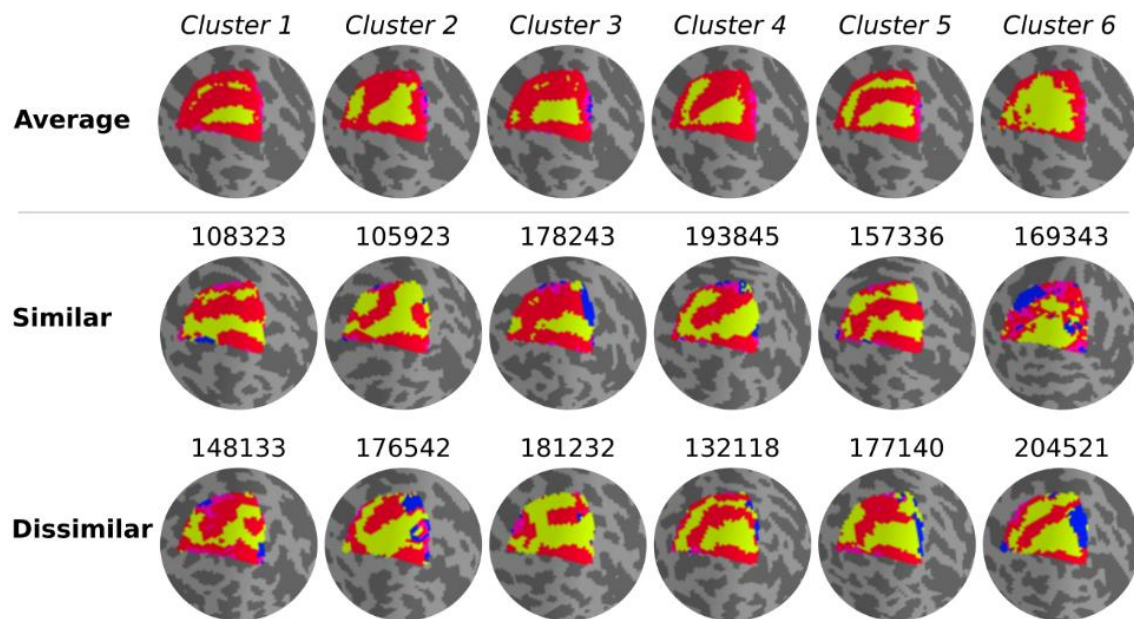
307 **Figure 3 - Clusters of retinotopic organization in the dorsal portion of early**  
308 **visual cortex. a,** Continuous polar angle maps were converted into discrete maps,  
309 such that each vertex would be categorized into one out of four possible labels. Spatial  
310 overlap between discrete maps was estimated using the Jaccard similarity coefficient  
311 from all possible pairs of individuals, resulting in a 181×181 similarity matrix. **b,** Then,  
312 we applied a spectral clustering algorithm – setting the number of clusters to 6. **c,** An  
313 average map (discrete and continuous) was calculated for each cluster by averaging  
314 the continuous polar angle maps across all individuals within each cluster.

315 Our findings clearly indicate shared patterns of retinotopic organization that deviate  
316 from the typical polar angle representation in the dorsal portion of early visual cortex

317 (Figure 1c). Specifically, average maps from clusters 1 and 5 capture nearly a third of  
318 individuals and show typical polar angle representations, with clear boundaries  
319 between V1/V2 and V2/V3 (Figure 1c and Figure 3c). However, clusters 2, 3, and 4  
320 capture nearly two thirds of individuals and deviate from this typical polar angle  
321 representation (Figure 3c). The average map from cluster 2 shows that the boundaries  
322 between V1 and V2, and the most anterior portion of V3 and higher-order visual areas,  
323 merge to form a Y-shaped (or forked) lower vertical representation. Clusters 3 and 4  
324 show a truncated V3 boundary, indicating that dorsal V3 does not cover the entire  
325 quarter visual field (i.e., from 360° to 270°) either throughout its length or only in its  
326 most anterior portion. Finally, cluster 6 reflects unclear retinotopic organization, with a  
327 handful of individuals' retinotopic maps showing overall low correspondence with the  
328 typical retinotopic organization.

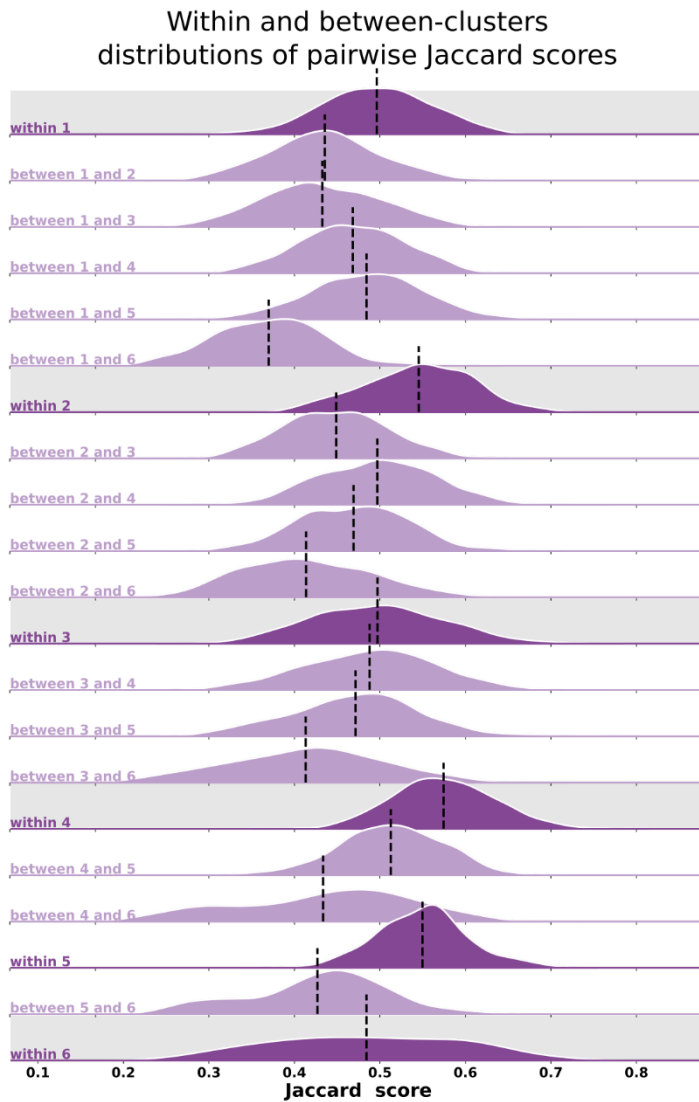
329 Qualitatively, individual maps seem to agree with their corresponding average cluster  
330 map, but there are some exceptions (Figure 4, Supplementary Figure 2). Figure 4  
331 shows the average cluster maps from each cluster and examples of individuals' maps  
332 that are qualitatively similar and dissimilar to their corresponding average cluster map.  
333 While most polar angle maps correspond well with their average cluster maps (as seen  
334 in the middle row of Figure 4), there is also an apparent mismatch between a few maps  
335 and their corresponding cluster average (bottom row in Figure 4). For example,  
336 individual #132118 was assigned to Cluster 4, but their polar angle map is qualitatively  
337 more similar to Cluster 5. These mismatches are likely due to the extensive overlap  
338 between within-cluster and between-clusters distributions of pairwise Jaccard scores  
339 (Figure 5). Note in Figure 5 that the within-cluster distributions highlighted in grey are  
340 generally shifted to the right compared to the between-clusters distributions, indicating  
341 their higher Jaccard scores. However, the overlap between these distributions is

342 substantial. For example, the between cluster 1 and 5 distribution overlaps with within-  
343 cluster 1 distribution throughout its entirety, which is justified by the significant  
344 similarity between their average maps. Despite this, we found that the average within-  
345 cluster Jaccard score is 0.54 (SD = 0.07), while the average between-clusters score  
346 is 0.46 (SD = .08), showing that pairs of maps within a cluster are, on average, more  
347 similar than between-clusters.



348

349 **Figure 4 - Qualitative evaluation of clusters.** Average cluster maps are shown in  
350 the top row. The middle row shows examples of maps from each cluster with a similar  
351 retinotopic organization to the corresponding average map. Finally, in the bottom row,  
352 examples of those with dissimilar organizations are shown.



353

354 **Figure 5 - Distributions of pairwise Jaccard scores.** Within and between-clusters  
355 distribution of Jaccard scores across all pairs of individuals. Within-cluster distributions  
356 are highlighted in grey. Between-clusters distributions are the same regardless of the  
357 order of the clusters, i.e., the Jaccard score distribution between cluster 1 and cluster  
358 2 ('between 1 and 2') is the same as the one between cluster 2 and 1. Black vertical  
359 lines indicate distributions' means.

## 360 Discussion

361 We systematically investigated individual variability in visual field representation of  
362 human early visual cortex using the HCP 7T retinotopy dataset. We found that  
363 retinotopic maps in the left hemisphere were more variable than those in the right

364 hemisphere. Moreover, in the left hemisphere the dorsal portions of early visual areas  
365 were more variable than their ventral counterparts. Additionally, we investigated  
366 whether there are common motifs in the observed individual variability in retinotopic  
367 maps. This analysis showed that deviations from the canonical model of continuous,  
368 alternating bands of vertical and horizontal meridian representation in V2 and V3 exist  
369 in the majority of individuals. Overall, our findings challenge the current view that the  
370 dorsal portions of early visual areas form retinotopic maps which are consistent  
371 between individuals as roughly mirror images of their ventral counterparts.

372 Although previous evidence for the variability seen across dorsal early visual cortex in  
373 humans has been mostly anecdotal, a number of studies have indicated a complex,  
374 retinotopic organization of dorsal early visual areas in non-human primates, using both  
375 electrophysiological recordings and high-resolution fMRI (Angelucci and Rosa, 2015;  
376 Gattass et al., 1988; Sereno et al., 2015; Zhu and Vanduffel, 2019). Accordingly, there  
377 is a long-standing debate about the number of visual areas – and their boundaries –  
378 in the third-tier visual cortex of New and Old-World monkeys (Angelucci and Rosa,  
379 2015; Hadjidimitrakis et al., 2019). However, the question of whether the areal  
380 boundaries in this region show significant individual variability has not been studied  
381 systematically in non-human primates. Only Gattass et al. (1988) reported, in the  
382 macaque monkey, that the representation of the lower vertical meridian in dorsal V3  
383 varied across individuals, but firm conclusions could not be drawn due to the small  
384 sample. These authors indicated that some animals showed a continuous  
385 representation of this meridian along the rostral border of this area, whereas in others  
386 additional field discontinuities created a discontinuous representation. Notably, the  
387 same discontinuities in the anterior border of dorsal V3 were also found in our  
388 systematic investigation of individual variability in human polar angle maps. It is also

389 significant that the same pattern of variation (relatively simple and reproducible  
390 representations of the upper contralateral quadrant, and complex and variable  
391 representations of the lower quadrant) characterize V2 and V3 in at least one non-  
392 primate, the cat (Rosa and Manger, 2005; Tusa et al., 1979). Overall, our findings in  
393 humans demonstrate that the organization of dorsal early visual areas is more  
394 heterogeneous than previously acknowledged and suggest that this may be a common  
395 feature of mammals with developed vision.

396 Although different models of third-tier visual cortex organization in non-human  
397 primates (Angelucci and Rosa, 2015) also suggest unusual eccentricity mapping, we  
398 did not find meaningful differences in clusters of eccentricity maps. This may be  
399 associated with the limited extent of the visual stimulus (up to 8° of eccentricity)  
400 (Benson et al., 2018) and remains to be further investigated. Another alternative is  
401 having a complex pattern of polar angle representation coexisting with a preserved  
402 eccentricity gradient, as demonstrated by previous work in areas V2 and V3 of cats  
403 (Tusa et al., 1979), flying foxes (Rosa, 1999), ferrets (Manger et al., 2002) and tree  
404 shrews (Sedigh-Sarvestani et al., 2021).

405 Our investigation provides firm evidence for individual variability in the retinotopic  
406 organization across parts of early visual areas in the human visual cortex. Moreover,  
407 the exploratory analysis indicates the presence of shared patterns of retinotopic  
408 organization that deviate from the typical polar angle representation in the dorsal  
409 portion of early visual cortex. Future work could extend these insights through  
410 additional analyses – for example, by employing different similarity metrics, using  
411 different features, or changing the number of clusters. Here, we limited our analysis to  
412 the spatial overlap of discrete polar angle maps, which means that a pair of  
413 qualitatively similar but spatially misaligned polar angle maps, for example, might have

414 a low Jaccard score. If another more suitable metric can consider the topographic  
415 organization of polar angle maps regardless of the spatial location, it would be possible  
416 to increase the consistency between an individual's map and their cluster average  
417 map. It would also be possible to estimate the similarity between two individuals'  
418 retinotopic maps from specific features extracted from the maps (such as linear  
419 magnification along isoeccentricity lines), to provide insights into changes in these  
420 properties as a function of cortical location (Schira et al., 2010). Finally, it is important  
421 to note that selecting the ideal number of clusters depends on the similarity metric  
422 employed, prior knowledge, and the clustering algorithm. Therefore, future work could  
423 be performed to explore the effect of the number of clusters on clustering quality  
424 (perhaps as indicated by within- vs. between-cluster similarity measures).

425 Given the presence of the variability across early visual cortex in humans, another  
426 potential line of investigation involves the origin of this variability. Pertinently, we  
427 recently developed a deep learning model of retinotopy able to predict this individual  
428 variability from individual-specific cortical curvature and myelin maps (Ribeiro et al.,  
429 2021), suggesting that it is a structure-related variation. In our subsequent work  
430 (Ribeiro et al., 2022), we further explored this model of retinotopy to unravel which  
431 anatomical feature (curvature or myelin) was the most important for individual  
432 variability in the dorsal portion of early visual cortex. Although we found neither feature  
433 was redundant, the model seems to be differentially relying on myelin feature maps to  
434 determine individual variability in the dorsal portion of early visual cortex. Studies  
435 modelling the formation of retinotopic maps in development have suggested that  
436 multistable solutions may occur depending on factors such as the degree of elongation  
437 of the area (Sedigh-Sarvestani et al., 2021; Wolf et al., 1994) and adjacency with other  
438 areas (Yu et al., 2020), which do not violate the need to minimize the length of

439 connections (Durbin and Mitchison, 1990; Swindale, 1996). Therefore, future work  
440 could evaluate whether there is an overlap between function- and anatomy-based  
441 clusters to help elucidate the developmental mechanisms underlying the variability of  
442 human dorsal extrastriate cortex.

443 Finally, another finding that requires consideration is the interhemispheric difference  
444 revealed in our data: retinotopic maps in the left hemisphere showed more variation  
445 than those in the right hemisphere. To date, there has been no report of  
446 interhemispheric differences in early visual cortex of other mammals, including non-  
447 human primates. In part, this may be traced to the relatively small samples in these  
448 studies, in comparison with those possible using human fMRI. However, another  
449 possibility is that such differences may arise more frequently in human brains, due to  
450 the scaling of callosal connections with brain size (Rilling and Insel, 1999), which may  
451 promote a higher degree of connective independence during development.

452 In conclusion, using a large-scale brain imaging dataset, we provide new insights into  
453 the variability in the topographical organization of human visual cortex. These insights  
454 may prove crucial in guiding further experimental investigations and theories about  
455 retinotopic organization differentiation across species, development, and individuals.

## 456 **Acknowledgments**

457 This work was supported by the Australian Research Council (DE180100433 and  
458 DP210101042). Data were provided by the Human Connectome Project, WU-Minn  
459 Consortium (Principal Investigators: David Van Essen and Kamil Ugurbil;  
460 1U54MH091657) funded by the 16 NIH Institutes and Centers that support the NIH  
461 Blueprint for Neuroscience Research; and by the McDonnell Center for Systems



462 Neuroscience at Washington University. In addition, FLR acknowledges support  
463 through the Australian Government Research Training Program Scholarship.

#### 464 **Competing financial interests**

465 The authors declare no competing financial interests.

#### 466 **References**

467 Abraham, A., Pedregosa, F., Eickenberg, M., Gervais, P., Mueller, A., Kossaifi, J.,  
468 Gramfort, A., Thirion, B., Varoquaux, G., 2014. Machine learning for neuroimaging  
469 with scikit-learn. *Front. Neuroinform.* 8, 1–10.  
470 <https://doi.org/10.3389/fninf.2014.00014>

471 Allen, E.J., St-Yves, G., Wu, Y., Breedlove, J.L., Prince, J.S., Dowdle, L.T., Nau, M.,  
472 Caron, B., Pestilli, F., Charest, I., Hutchinson, J.B., Naselaris, T., Kay, K., 2021.  
473 A massive 7T fMRI dataset to bridge cognitive neuroscience and artificial  
474 intelligence. *Nat. Neurosci.* <https://doi.org/10.1038/s41593-021-00962-x>

475 Angelucci, A., Rosa, M.G.P., 2015. Resolving the organization of the third tier visual  
476 cortex in primates: A hypothesis-based approach. *Vis. Neurosci.* 32.  
477 <https://doi.org/10.1017/S0952523815000073>

478 Arcaro, M.J., Kastner, S., 2015. Topographic organization of areas V3 and V4 and its  
479 relation to supra-areal organization of the primate visual system. *Vis. Neurosci.*  
480 <https://doi.org/doi:10.1017/S0952523815000115>

481 Benson, N.C., Butt, O.H., Brainard, D.H., Aguirre, G.K., 2014. Correction of Distortion  
482 in Flattened Representations of the Cortical Surface Allows Prediction of V1-V3  
483 Functional Organization from Anatomy. *PLoS Comput. Biol.* 10.

- 484 <https://doi.org/10.1371/journal.pcbi.1003538>
- 485 Benson, N.C., Butt, O.H., Datta, R., Radoeva, P.D., Brainard, D.H., Aguirre, G.K.,  
486 2012. The retinotopic organization of striate cortex is well predicted by surface  
487 topology. *Curr. Biol.* 22, 2081–2085. <https://doi.org/10.1016/j.cub.2012.09.014>
- 488 Benson, N.C., Jamison, K.W., Arcaro, M.J., Vu, A.T., Glasser, M.F., Coalson, T.S.,  
489 Van Essen, D.C., Yacoub, E., Ugurbil, K., Winawer, J., Kay, K., 2018. The Human  
490 Connectome Project 7 Tesla retinotopy dataset: Description and population  
491 receptive field analysis. *J. Vis.* 18, 1–22.
- 492 Benson, N.C., Winawer, J., 2018. Bayesian analysis of retinotopic maps. *Elife* 7, 1–  
493 29. <https://doi.org/10.7554/elife.40224>
- 494 Dumoulin, S.O., Wandell, B.A., 2008. Population receptive field estimates in human  
495 visual cortex. *Neuroimage* 39, 647–660.  
496 <https://doi.org/10.1016/j.neuroimage.2007.09.034>
- 497 Durbin, R., Mitchison, G., 1990. A dimension reduction framework. *Nature* 343, 644–  
498 647.
- 499 Gattass, R., Gross, C.G., Sandell, J.H., 1981. Visual topography of V2 in the macaque.  
500 *J. Comp. Neurol.* 201, 519–539. <https://doi.org/10.1002/cne.902010405>
- 501 Gattass, R., Sousa, A.P.B., Gross, C.G., 1988. Visuotopic organization and extent of  
502 V3 and V4 of the macaque. *J. Neurosci.* 8, 1831–1845.  
503 <https://doi.org/10.1523/jneurosci.08-06-01831.1988>
- 504 Glasser, M.F., Coalson, T.S., Robinson, E.C., Hacker, C.D., Harwell, J., Yacoub, E.,  
505 2016. A multi-modal parcellation of human cerebral cortex. *Nature* 536, 171–178.  
506 <https://doi.org/10.1038/nature18933>

- 507 Glasser, M.F., Sotiropoulos, S.N., Wilson, J.A., Coalson, T.S., Fischl, B., Andersson,  
508 J.L., Xu, J., Jbabdi, S., Webster, M., Polimeni, J.R., Van Essen, D.C., Jenkinson,  
509 M., 2013. The minimal preprocessing pipelines for the Human Connectome  
510 Project. *Neuroimage* 80, 105–124.  
511 <https://doi.org/10.1016/j.neuroimage.2013.04.127>
- 512 Hadjidimitrakis, K., Bakola, S., Chaplin, T.A., Yu, H.H., Alanazi, O., Chan, J.M.,  
513 Worthy, K.H., Rosa, M.G.P., 2019. Topographic organization of the ‘third-tier’  
514 dorsomedial visual cortex in the macaque. *J. Neurosci.* 39, 5311–5325.  
515 <https://doi.org/10.1523/JNEUROSCI.0085-19.2019>
- 516 Kay, K.N., Winawer, J., Mezer, A., Wandell, B.A., 2013. Compressive spatial  
517 summation in human visual cortex. *J. Neurophysiol.* 110, 481–494.  
518 <https://doi.org/10.1152/jn.00105.2013>
- 519 Levandowsky, M., Winter, D., 1971. Distance between sets. *Nature* 234, 34–35.  
520 <https://doi.org/10.1038/234034a0>
- 521 Luxburg, U. Von, 2007. A tutorial on spectral clustering. *Stat. Comput.* 17, 395–416.  
522 <https://doi.org/10.1007/s11222-007-9033-z>
- 523 Magezi, D.A., 2015. Linear mixed-effects models for within-participant psychology  
524 experiments: An introductory tutorial and free, graphical user interface (LMMgui).  
525 *Front. Psychol.* 6, 1–7. <https://doi.org/10.3389/fpsyg.2015.00002>
- 526 Manger, P.R., Kiper, D., Masiello, I., Murillo, L., Tettoni, L., Hunyadi, Z., Innocenti,  
527 G.M., 2002. The Representation of the Visual Field in Three Extrastriate Areas of  
528 the Ferret (*Mustela putorius*) and the Relationship of Retinotopy and Field  
529 Boundaries to Callosal Connectivity. *Cereb. Cortex* 12, 423–437.  
530 <https://doi.org/10.1093/cercor/12.4.423>

- 531 Pedregosa, F., Varoquaux, G., Gramfort, A., Michel, V., Thirion, B., Grisel, O., Blondel,  
532 M., Prettenhofer, P., Weiss, R., Dubourg, V., Vanderplas, J., Passos, A.,  
533 Cournapeau, D., Brucher, M., Perrot, M., Duchesnay, E., 2011. Scikit-learn:  
534 Machine Learning in Python. *J. Mach. Learn. Res.* 12, 2825–2830.
- 535 Ribeiro, F.L., Bollmann, S., Cunnington, R., Puckett, A.M., 2022. An explainability  
536 framework for cortical surface-based deep learning. *arXiv* 1–10.
- 537 Ribeiro, F.L., Bollmann, S., Puckett, A.M., 2021. Predicting the retinotopic organization  
538 of human visual cortex from anatomy using geometric deep learning. *Neuroimage*  
539 244, 118624. <https://doi.org/10.1016/j.neuroimage.2021.118624>
- 540 Rilling, J.K., Insel, T.R., 1999. Differential expansion of neural projection systems in  
541 primate brain evolution. *Neuroreport* 10, 1453–1459.  
542 <https://doi.org/10.1097/00001756-199905140-00012>
- 543 Rosa, M.G.P., 2002. Visual maps in the adult primate cerebral cortex: some  
544 implications for brain development and evolution. *Brazilian J. Med. Biol. Res.* 35,  
545 1485–1498. <https://doi.org/10.1590/S0100-879X2002001200008>
- 546 Rosa, M.G.P., 1999. Topographic organisation of extrastriate areas in the flying fox:  
547 Implications for the evolution of mammalian visual cortex. *J. Comp. Neurol.* 411,  
548 503–523. [https://doi.org/10.1002/\(SICI\)1096-9861\(19990830\)411:3<503::AID-  
549 CNE12>3.0.CO;2-6](https://doi.org/10.1002/(SICI)1096-9861(19990830)411:3<503::AID-CNE12>3.0.CO;2-6)
- 550 Rosa, M.G.P., Manger, P.R., 2005. Clarifying homologies in the mammalian cerebral  
551 cortex: The case of the third visual area (V3). *Clin. Exp. Pharmacol. Physiol.* 32,  
552 327–339. <https://doi.org/10.1111/j.1440-1681.2005.04192.x>
- 553 Schira, M.M., Tyler, C.W., Breakspear, M., Spehar, B., 2009. The foveal confluence in

- 554 human visual cortex. *J. Neurosci.* 29, 9050–9058.  
555 <https://doi.org/10.1523/JNEUROSCI.1760-09.2009>
- 556 Schira, M.M., Tyler, C.W., Spehar, B., Breakspear, M., 2010. Modeling magnification  
557 and anisotropy in the primate foveal confluence. *PLoS Comput. Biol.* 6, 1–10.  
558 <https://doi.org/10.1371/journal.pcbi.1000651>
- 559 Sedigh-Sarvestani, M., Lee, K.-S., Jaepel, J., Satterfield, R., Shultz, N., Fitzpatrick, D.,  
560 2021. A sinusoidal transformation of the visual field is the basis for periodic maps  
561 in area V2. *Neuron* 109, 4068-4079.e6.  
562 <https://doi.org/10.1016/j.neuron.2021.09.053>
- 563 Sereno, M.I., McDonald, C.T., Allman, J.M., 2015. Retinotopic organization of  
564 extrastriate cortex in the owl monkey—dorsal and lateral areas. *Vis. Neurosci.* 32,  
565 E021. <https://doi.org/10.1017/S0952523815000206>
- 566 Swindale, N. V, 1996. The development of topography in the visual cortex: a review of  
567 models. *Network* 7, 161–247. <https://doi.org/10.1088/0954-898X/7/2/002>
- 568 Taha, A.A., Hanbury, A., 2015. Metrics for evaluating 3D medical image segmentation:  
569 Analysis, selection, and tool. *BMC Med. Imaging* 15.  
570 <https://doi.org/10.1186/s12880-015-0068-x>
- 571 The jamovi project (2021), n.d.
- 572 Tusa, R.J., Rosenquist, A.C., Palmer, L.A., 1979. Retinotopic organization of areas 18  
573 and 19 in the cat. *J. Comp. Neurol.* 185, 657–678.  
574 <https://doi.org/10.1002/cne.901850405>
- 575 Van Essen, D.C., Glasser, M.F., 2018. Parcellating Cerebral Cortex: How Invasive  
576 Animal Studies Inform Noninvasive Mapmaking in Humans. *Neuron* 99, 640–663.

- 577 <https://doi.org/10.1016/j.neuron.2018.07.002>
- 578 Van Essen, D.C., Smith, S.M., Barch, D.M., Behrens, T.E.J., Yacoub, E., Ugurbil, K.,  
579 2013. The WU-Minn Human Connectome Project: An overview. *Neuroimage* 80,  
580 62–79. <https://doi.org/10.1016/j.neuroimage.2013.05.041>
- 581 Wandell, B.A., Winawer, J., 2010. Imaging retinotopic maps in the human brain. *Vision*  
582 *Res.* 51, 718–737. <https://doi.org/10.1016/j.visres.2010.08.004>.Imaging
- 583 Wang, L., Mruczek, R.E.B., Arcaro, M.J., Kastner, S., 2015. Probabilistic maps of  
584 visual topography in human cortex. *Cereb. Cortex* 25, 3911–3931.  
585 <https://doi.org/10.1093/cercor/bhu277>
- 586 Wolf, F., Bauer, H.U., Geisel, T., 1994. Formation of field discontinuities and islands  
587 in visual cortical maps. *Biol. Cybern.* 70, 525–531.  
588 <https://doi.org/10.1007/BF00198805>
- 589 Yu, H.H., Rowley, D.P., Price, N.S.C., Rosa, M.G.P., Zavitz, E., 2020. A twisted visual  
590 field map in the primate cortex predicted by topographic continuity. *Sci. Adv.*  
591 <https://doi.org/10.1101/682187>
- 592 Yu, Z., Guindani, M., Grieco, S.F., Chen, L., Holmes, T.C., Xu, X., 2022. Primer  
593 Beyond t test and ANOVA : applications of mixed-effects models for more rigorous  
594 statistical analysis in neuroscience research. *Neuron* 110, 21–35.  
595 <https://doi.org/10.1016/j.neuron.2021.10.030>
- 596 Zhu, Q., Vanduffel, W., 2019. Submillimeter fMRI reveals a layout of dorsal visual  
597 cortex in macaques, remarkably similar to New World monkeys. *Proc. Natl. Acad.*  
598 *Sci. U. S. A.* 116, 2306–2311. <https://doi.org/10.1073/pnas.1805561116>